ROYAL SOCIETY OF CHEMISTRY

PAPER

Check for updates

532- and 52-symmetric Au helicoids synthesized through controlled seed twinning and aspect ratio†

Jack S. Googasian, [ID] Maxwell P. Perkins, [ID] Jun Chen and Sara E. Skrabalak [ID] *

Chiral plasmonic crystals with 5-fold symmetries were synthesized from Au icosahedra, decahedra, and pentatwinned nanorods, unraveling the effects of seed twinning and aspect ratio on chiral overgrowth directed by L-glutathione. The influence of seed size on the overgrowth from pentatwinned nanorods was also studied, giving insight into the role volumetric strain plays in chiral crystal formation. Single particle reconstructions were obtained using electron tomography, and optical simulations on the measured structures verify their optical chirality.

Introduction

Chirality emerges at many length scales, from single molecules to the macroscopic world. Nanomaterials are no exception, with chiral materials being achieved by both top-down and bottom-up methods.[1–4] Colloidal synthesis has been used to make chiral metal nanocrystals (NCs),[5–9] with those composed of Au and Ag garnering attention for their strong light–matter interactions, which result from their ability to sustain a localized surface plasmon resonance (LSPR).[10] Such plasmonic NCs are intriguing given the possibility of enantioselective light–matter interactions.[1,11–15]

Seed-mediated growth approaches are state-of-the-art, where simple chiral molecules serve as shape-directing agents during overgrowth to achieve chiral NCs with varying symmetry.[6,7,13,16–18] Recall the pioneering studies by Lee *et al.* where Au was deposited on single-crystalline Au seeds of octahedral and cubic shapes in the presence of L-glutathione (L-GSH) or L-cysteine (L-cys), and the resulting NCs displayed the rotational symmetry of the initial seeds but lost mirror symmetry.[13] The chiral molecules that served as shape-directing agents are hypothesized to impart their chirality through binding at kink sites on the seed surfaces,[13] *i.e.*, high-Miller index sites at the intersection of the three most thermodynamically stable facets: {111}, {100}, and {110}.[13,19,20]

Seeds with single twin defects have also been studied, with irregular, anisotropic morphologies generated that were

Department of Chemistry, Indiana University – Bloomington, 800 E Kirkwood Ave, Bloomington, IN 47405, USA. E-mail: sskrabal@iu.edu
†Electronic supplementary information (ESI) available. See DOI: https://doi.org/10.1039/d4nr03731f

expected to hamper the sample's g-factor,[13] which is defined as the preferential interaction with left circularly polarized (LCP) or right circularly polarized (RCP) light (eqn (1)):

$$g\text{-Factor} = \frac{2(A_L - A_R)}{(A_L + A_R)} \propto \frac{\text{CD}}{\text{extinction}} \tag{1}$$

where CD is the difference in extinction from circular dichroism (CD) spectroscopy, and A_L and A_R represent the absorbance of left- and right-circularly polarized light.

Since then, the field has intentionally studied a variety of seed shapes with twin planes and stacking faults, with chiral NCs of different symmetries achieved.[6,7,17,21,22] For example, chiral helicoids with tetrahedral and 3-fold dihedral rotational symmetry were achieved from overgrowth on Au tetrahedral and triangular plate seeds.[6] Also, homochiral Au nanopropellers were reported from overgrowth of decahedral (pentatwinned) seeds in the presence of D-glutathione.[17,23] Chirality was found to depend on the relative ratio of seeds to overgrowth solution. Here, we report 532- and 52-symmetric Au helicoids from ($\bar{5}\bar{3}m$) icosahedral and ($\overline{10}m2$) pentatwinned seeds, where the seed symmetry directs the number and symmetry of branches in the chiral helicoid product. Note that this symmetry notation is for the idealized symmetry and does not account for slight variations and imperfections present in "real world" crystals. In addition to seed symmetry, the growth mode of the chiral 52-symmetric helicoids was found to depend on seed size, where larger seeds produce isolated branches with deep chiral gaps and smaller seeds produce elongated bipyramids with indentations along the faces. This difference highlights the role of volumetric strain in the synthesis of chiral particles from twinned seeds.

Experimental

Materials

Gold(III) chloride trihydrate ($HAuCl_4 \cdot 3H_2O$, ≥99.9%), L-ascorbic acid (L-AA, BioXtra, ≥99.0%), hexadecyltrimethylammonium bromide (CTAB, BioUltra, ≥99.0%), cetyltrimethylammonium chloride solution (CTAC, 25 wt% in H_2O), sodium citrate tribasic dihydrate ($Na_3Citrate \cdot 2H_2O$, BioUltra, ≥99.5%), L-glutathione reduced (L-GSH, ≥98%), silver nitrate ($AgNO_3$, 99.9999%), polyvinylpyrrolidone (PVP55, average M_w ~55 000), N,N-dimethylformamide (DMF, 99.9%), and sodium borohydride ($NaBH_4$, 99.99%) were purchased from Sigma Aldrich. Benzyldimethyl ammonium chloride (BDAC, 95%) was purchased from Alfa Aesar. CTAB was recrystallized three times before use; all other chemicals were used as received. All solutions were prepared with nanopure (18.2 MΩ cm) water.

Synthesis overview

The 532- and 52- helicoids were synthesized from icosahedral and pentatwinned seeds (decahedra and nanorods), respectively. First, the syntheses of the seeds are presented, then the overgrowth procedures.

Synthesis of icosahedral seeds

The icosahedral seeds used for the synthesis of 532- helicoids were prepared by first preparing small icosahedral seeds then growing them to a larger size.

The synthesis of small icosahedral seeds was adapted from literature as follows:[24]

Step 1: To a 30 mL vial, a growth mixture of 75 μL $HAuCl_4$ (26 mM), 14.5 μL $AgNO_3$ (100 mM), 140 μL nanopure water, 480 mg PVP55, and 3 mL DMF was prepared. The vial was heated in an oil bath at 120 °C with gentle stirring for 60 minutes.

Step 2: While the vial containing the growth mixture was cooling, 375 μL $HAuCl_4$ (26 mM), 625 μL nanopure water, and 1.2 g of PVP55 were dissolved in 15 mL of DMF in a separate vial. This mixture was heated at 120 °C with gentle stirring for 10 minutes.

Step 3: 500 μL of the growth solution from Step 1 was added to the reaction mixture from Step 2 while continuing to heat and stir. The vial was left in an oil bath at 120 °C with gentle stirring for 60 minutes, then cooled to room temperature. These small icosahedral seeds were then stored as synthesized without further purification.

The small icosahedral seeds were then grown to larger size using a literature procedure.[25] To a 30 mL vial, 5 mL of nanopure water, 100 μL of $HAuCl_4$ (50 mM), and 5 mL BDAC (200 mM) were added. 75 μL of freshly prepared L-AA (100 mM) was then added. When the solution went from faint yellow to clear, 500 μL of the small icosahedral seed solution was added. The reaction vial was added to an oil bath at 30 °C for 2 hours, with the product collected via centrifugation (11 400 RCF, 10 min) and the supernatant being discarded. The collected pellet of icosahedral seeds was redispersed in 1 mL nanopure water for further characterization.

Synthesis of pentatwinned seeds

5 different seeds were prepared with a pentatwinned cross-section and used in chiral particle growth. These include large pentatwinned rods (width = ~80–100 nm) with aspect ratios (ARs) of ~1 (decahedra), 1.5, and 2.2 as well as small pentatwinned rods (width = ~20 nm) and ARs of 2.2 and 3.2.

The large pentatwinned rods (AR = ~1) were synthesized from a literature approach by first preparing small decahedral seeds and growing them to larger size.[25]

Step 1: To a 30 mL vial, 2.5 mL of water, 2.5 mL of $HAuCl_4$ (1 mM), 2.5 mL of CTAC (200 mM), and 2.5 mL of sodium citrate (20 mM) were added. The solution was stirred at 1000 rpm and allowed to mature while $NaBH_4$ (25 mM) solution was prepared with ice-cold water. 250 μL of freshly prepared $NaBH_4$ was quickly added to the reaction vial and the solution was stirred for 2 minutes uncapped. After two minutes, the reaction vial was capped and suspended in an oil bath at 80 °C with gentle stirring for 90 minutes. These seeds were then used in the next step prepared, without further purification.

Step 2: To a 30 mL vial, 5 mL of nanopure water, 100 μL of $HAuCl_4$ (50 mM), and 5 mL of BDAC (200 mM) were added. 75 μL of L-AA (100 mM) was then added. When the solution went from faint yellow to clear, 25 μL of pentatwinned seed solution from Step 1 was added. The reaction vial was added to an oil bath at 30 °C for 2 hours, then the product was collected via centrifugation (11 400 RCF, 10 min), with the supernatant being discarded. The collected NC pellet was redispersed in 1 mL nanopure water for further characterization.

The large pentatwinned rods with ARs of 1.5 and 2.2 were synthesized from an adapted protocol.[26] 15 mg CTAB were dissolved in 10 mL of nanopure water. Next, 5 mL of this CTAB solution was added to 5 mL CTAC (200 mM) in a 30 mL vial and left stirring at 30 °C for 10 minutes. Next, a given volume of $HAuCl_4$ (100 mM) was added, and the solution was stirred for 15 minutes. A volume of L-AA (100 mM) was then added, followed by 40 μL of the large pentatwinned rod (AR = ~1) solution. The solution was stirred vigorously (1000 rpm) for 30 seconds, then the vial was added to an oil bath at 30 °C for 1 hour. The large pentatwinned nanorods were then recollected via centrifugation (11 400 RCF, 10 min), with the supernatant being discarded. The collected NC pellet was redispersed in 1 mL nanopure water for further characterization. The synthesis conditions for each sample are summarized in Table 1.

The synthesis of small pentatwinned rods (width = ~20 nm) with ARs of 2.2 and 3.2 was adapted from literature.[26] 15 mg CTAB were dissolved in 10 mL of nanopure water. Next, 5 mL

Table 1 Synthesis conditions for large (width = ~80–100 nm) pentatwinned rods with AR 1.5 and 2.2

Fig.	$HAuCl_4$ volume (μL)	L-AA volume (μL)
3b	8.3	12.5
3c	25	37.5

of this CTAB solution was added to 5 mL CTAC (200 mM) in a 30 mL vial and left stirring at 30 °C for 10 minutes. Next, 33.35 μL $HAuCl_4$ was added, and the solution was stirred for 15 minutes. 12.5 μL of L-AA (100 mM) was then added, followed by 25 μL of the small pentatwinned seed solution (from Step 1 of large pentatwinned rods (AR = ~1) synthesis). The solution was stirred vigorously (1000 rpm) for 30 seconds, then the vial was added to an oil bath at a set temperature for 1 hour. The product was then collected *via* centrifugation (11 400 RCF, 10 min), with the supernatant being discarded. The collected NC pellet was redispersed in 1 mL nanopure water for further characterization. The synthesis conditions for each sample are summarized in Table 2.

Synthesis of 532- and 52- symmetric helicoids

The procedure for chiral overgrowth from Au seeds was adapted from previous work.[13] To a 30 mL vial, 3.95 mL of nanopure water, 200 μL $HAuCl_4$ (10 mM), and 800 μL of CTAB (100 mM) were added. The reaction mixture was swirled to mix the reagents. Next, 475 μL L-AA (100 mM) was added followed by 5 μL L-GSH (5 mM). Finally, a specific volume of Au NC seed solution was added and swirled, then the vial was suspended in an oil bath at 30 °C for 2 h. The product was collected by centrifugation of the reaction solution (11 400 RCF, 10 min), with the supernatant being discarded. The collected pellet of particles were re-dispersed in 1 mL nanopure water for further characterization. The synthesis conditions for each sample are summarized in Table 3.

General particle characterization

CD and UV-visible extinction measurements were acquired using a Jasco J-715 circular dichroism spectropolarimeter in a quartz cuvette with a path length of 1 cm and sample channel of 1 cm at room temperature. Optical characterizations were corrected to water background. Samples for scanning electron microscopy (SEM) imaging were prepared by

Table 2 Synthesis conditions for small pentatwinned rods (width = ~20 nm) with AR 2.2 and 3.2

Fig.	Temperature (°C)	Pentatwinned seed volume (μL)
5a	80	12.5
5b	30	25.0

Table 3 Synthetic conditions for 532- and 52- symmetric helicoids

Fig.	Seed volume (μL)
1a	124.5
1b	83.0
1c	41.5
3d	50.0
3e	200.0
3f	200.0
5c	50.0
5d	50.0

drop-casting particle solutions onto pre-cut Si wafer stubs. After allowing the droplets to dry, the stubs were cleaned by flushing the surface and drawing up small quantities of ethanol several times before imaging. SEM images were obtained with a FEI Quanta FEG 600 field-emission environmental scanning electron microscope or a Zeiss Auriga 60 focused ion beam-scanning electron microscope. Both operated at 30 kV with a spot size of 3. For tilt studies, the Zeiss Auriga 60 focused ion beam-scanning electron microscope was operated at 30 kV with a spot size of 3, and images were acquired at 0°, 15°, 30°, and 45°.

Tomography acquisition and reconstruction details

Transmission electron microscopy (TEM) samples were prepared by drop-casting 10 μL of aqueous particle solutions onto a carbon-coated copper grid. Data was acquired on a JEOL 3200 operating at 300 keV. For each sample, 60 STEM-HAADF images were acquired, with steps of 2° between ±60°. Tilt series alignment was performed by applying cross-correlation followed by tilt-axis rotation/shift alignment using tomviz software. Tomographic reconstruction was performed using TV minimization method with 10 iterations using tomviz software.[27] Intensity thresholding and segmentation was performed using Amira software to generate the isosurfaces.

Finite difference time domain (FDTD) simulations

FDTD simulations were performed using Lumerical FDTD Solutions software. The refractive index was set to 1.333. The dielectric functions for the models were fit to optical data collected by Johnson and Christy.[28] The mesh cells were set to 4 nm to limit simulation time. The left or right circularly polarized (LCP/RCP) source was generated by using two linearly polarized light Total Field Scattered Field sources that are mutually perpendicular along the propagation direction (*z*-axis), offset by 90° phase difference with a wavelength range of 300–1000 nm. STL files were generated from the tomographical reconstructions and imported into the Lumerical software, scaling properly for reconstructed particle size. Two simulations (one with LCP and one with RCP) were conducted, and the *g*-factor was then calculated from these results. To accurately represent random orientation in solution, the reconstruction was rotated in the *x*- and *y*-axes from 0–180° in steps of 15°. The final *g*-factor was obtained by averaging across all orientations.

Results and discussion

Icosahedral Au seeds were synthesized to investigate the effect of twinning on chiral overgrowth (Fig. S1a†). These seeds were then added to a chiral growth solution in which $HAuCl_4$ was reduced by L-AA in the presence of BDAC. The resulting particles exhibit high degrees of branching from icosahedral seeds where the branches are all slightly twisted, indicative of symmetry transfer from $\bar{5}\bar{3}m$-symmetric seeds to 532-symmetric products (Fig. 1). Therefore, these products will be referred to as 532-symmetric helicoids. As the concentration of

Fig. 1 Structural and optical characterization of 532-symmetric Au helicoids grown from icosahedral seeds. (a–c) SEM images of 532-symmetric helicoids. (d–f) Graphs of experimental UV-visible *g*-factor (red) and normalized extinction (black) spectra *versus* wavelength for the 532-symmetric helicoids. The icosahedral seed volumes added to the growth solution for samples (a–c) were 124.5, 83, and 41.5 µL, respectively.

seeds used in the chiral growth step decreased, the size of the 532-symmetric helicoids increased (Fig. 1a–c). Regardless of size, the branches that give rise to particle chirality are well separated, likely owing to enhanced adsorption of chiral molecules at the twin planes where high Miller index kink sites, (*i.e.*, the chiral intersection of {111}, {100}, and {110} facets), are likely to form.[13]

The optical properties of the 532-symmetric helicoids were investigated by UV-visible and CD spectroscopy, with results shown in Fig. 1d–f. As the seed concentration decreased, the branch length, particle size, and *g*-factor all increased. Consistent with previous results that showed chiral overgrowth on tetrahedral and triangular plate seeds,[6] the icosahedral seeds do not exhibit a *g*-factor response, (Fig. S1b†), which suggests the chiral response is due to the 532-symmetric helicoid structures.

The measured *g*-factor of these samples appears to be rather low when compared with other chiral nanocrystals,[6,7,13] but there are structural impurities which complicate assignment of the optical response to the particles grown from icosahedra. Although bulk measurements of randomly oriented colloidal solutions are free from linear dichroism effects such as in thin films, they are unable to distinguish between particles of interest and byproducts. Thus, single-particle studies were undertaken (Fig. 2). Specifically, tomographic reconstructions of two helicoids were obtained and are shown in Fig. 2b and e, corresponding to the samples in Fig. 1a and c, respectively. Both particles exhibit icosahedral diffraction patterns that
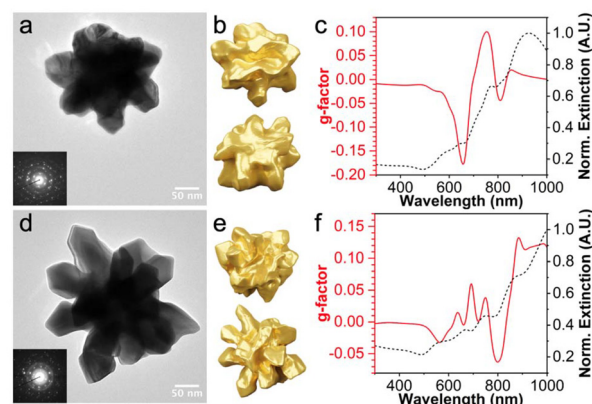
Fig. 2 (a and d) TEM images (insets: electron diffraction, corrected for brightness/contrast), (b and e) tomographic reconstructions, and (c and f) graphs of simulated *g*-factor (red trace) and normalized scattering (black trace) spectra *versus* wavelength of single 532-symmetric Au helicoids. Tomogram scale bars: 100 nm. Characterization in (a–c) and (d–f) correspond to representative helicoids from Fig. 1a and c, respectively.

confirm their underlying icosahedral twinning, with the particles in Fig. 2a and d oriented along the 3- and 5-fold axes, respectively.

Next, the *g*-factor and extinction spectra were calculated for these reconstructions *via* FDTD calculations and are shown in Fig. 2c and f. There are slight differences between the simulated and experimental spectra which are likely due to particle

averaging, structural impurities, and/or polydispersity as the simulated spectra are more intense than the experimental data; however, both simulated spectra match the position and sign of g-factor responses which suggests that the tomograms represent the particle types responsible for the measured g-factor. Additionally, there are multiple individual g-factor peaks in the simulated spectra which all have a corresponding extinction peak while the experimental spectra are broader. This difference is consistent with polydispersity.

Generally, seeds direct branching symmetry during overgrowth, which was evident in the growth of chiral NCs from single-crystalline seeds of lower symmetry (e.g., octahedra and tetrahedra).[4,29] Therefore, pentatwinned seeds of ($\overline{10}m2$) symmetry were also used to study the roles of symmetry and seed twinning on chiral overgrowth. Specifically, we hypothesized that if 52-symmetric dihedral seeds were used in chiral particle synthesis, then the overgrowth would exhibit fewer branches than in the icosahedral seed example and be directed by the twin defects within the seeds.

Toward this end, large Au pentatwinned rods (width = ~80–100 nm) of varying aspect ratio (AR) (~1, 1.5, and 2.2 shown in Fig. 3a–c respectively) were synthesized. They were then used as seeds in which HAuCl$_4$ was reduced by L-AA in the presence of CTAB and L-GSH, producing rod-like particles with each rod end displaying a 5-fold counterclockwise pinwheel ends (Fig. 3d–f). These 52-symmetric helicoids were further characterized through a series of tilted SEM images (Fig. S2†), which reveals deep grooves along their long axes as well.[13]

The helicoids grown from pentatwinned Au rods with AR ~1, are larger than the seeds, with an increase in AR as well. This observation is consistent with capping of CTAB on the {100} facets facilitating deposition preferentially to the {111} facets of the seeds as well as minimization of interfacial strain along the twin boundaries (C_2 axes).[30] These results are consistent with previous research investigating defect-directed seeded growth in which symmetrically branched NCs were achieved with transfer of seed symmetry.[31]
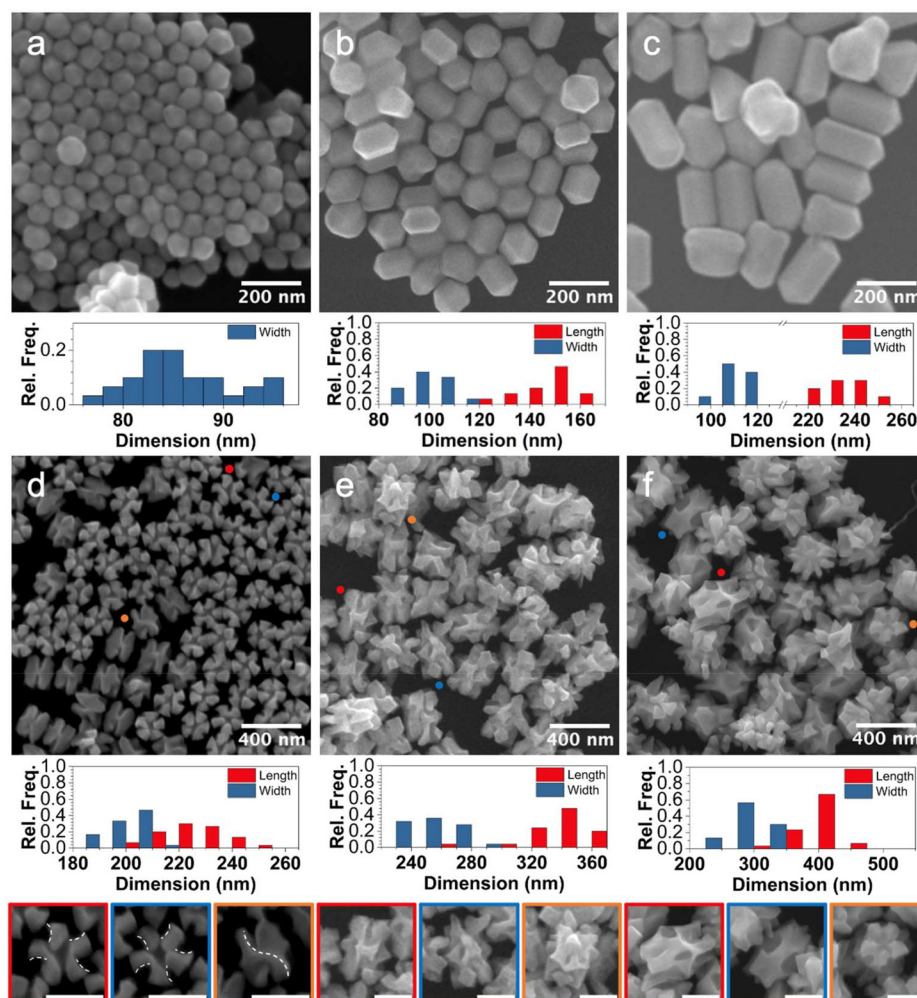
Fig. 3 (a–c) SEM images of large pentatwinned rods (width = ~80–100 nm) used as seeds, with AR = ~1, 1.5, and 2.2, respectively, and (d–f) SEM images of 52-symmetric helicoids. Size distribution histograms for each sample are shown below the respective SEM image, and selected helicoids (indicated by colored dots) are shown at the bottom of each respective column (scale bars: 200 nm).

Notably, the helicoids grown from pentatwinned Au NCs with AR 1.5 and 2.2, while larger than the seeds, decrease in AR. Similar pinwheel-capped rod ends are observed, along with concavities around the former dihedral mirror plane of the seeds (Fig. S2;† note that the 52-helicoid particles eliminate mirror symmetry during overgrowth, with the dihedral mirror plane merely serving as a reference point). The concavities may arise as a strain relief mechanism as suggested by work by Smith *et al.*[31]

The samples containing the 52-symmetric Au helicoids also exhibit chiroptical activity (Fig. 4). The optical properties of the 52-symmetric helicoids were investigated by UV-visible and CD spectroscopy (Fig. 4a, d and g). The *g*-factor of the product increases when increasing the seed AR from ~1 to 1.5 (Fig. 4a *versus* Fig. 4d); however, increasing extinction with particle size leads to a decrease in *g*-factor for the 52-helicoids seeded from AR 2.2 seeds (Fig. 4g). The optical spectra for helicoids from AR 1.5 seeds show a multimodal CD interaction, suggesting that the growth around the dihedral plane either generates chiral features of a different length scale or the larger size supports higher-order plasmon modes.[32] Note that the seeds do not show any chiroptic activity (Fig. S3†), indicating that these responses result from product particles.

To ensure that the chiroptical response of the samples arises from the 52-symmetric helicoids and not impurity structures, electron tomograms were collected of each structure, shown in Fig. 4b, e and h. FDTD simulations were then conducted using the reconstructions as models (Fig. 4c, f and i).

The numerical results show good agreement with the experimental spectra in terms of band position, sign, and shape, though some slight discrepancies exist likely due to particle-to-particle heterogeneity or impurity products. For example, the experimental data show negative *g*-factor peaks around 575, 700, and 625 nm for Fig. 4a, d and g and have matching simulated *g*-factor peaks in the simulated spectra around 600, 680, and 600 nm in Fig. 4c, f and i, respectively. This finding suggests that the tomograms accurately resemble the 52-symmetric helicoids in solution. The *g*-factor of each sample is relatively weak, which is consistent for large particles of similar dihedral systems.[6,7,17]

Previous research has shown that the *g*-factor response of chiral NCs can be increased by over 300% through synthetic optimization.[6] We anticipate that the 52-symmetric helicoids could benefit from such treatment. However, if helicoid formation is limited to large particle sizes, a very strong chiroptical response may not be possible as extinction increases with size (see eqn (1)). With this limitation in mind, we sought to synthesize the 52-symmetric helicoids from smaller pentatwinned rods as seeds.

Specifically, small pentatwinned Au rods (width = ~20 nm) and ARs of 2.2 and 3.2 (Fig. 5a and b) were synthesized then used as seeds in the chiral growth solution, where $HAuCl_4$ was reduced with L-AA in the presence of CTAB and L-GSH. Bipyramid-like particles with concave features emanating from their dihedral planes to tip form, as shown in Fig. 5c and d. These structures are in stark contrast to the particles
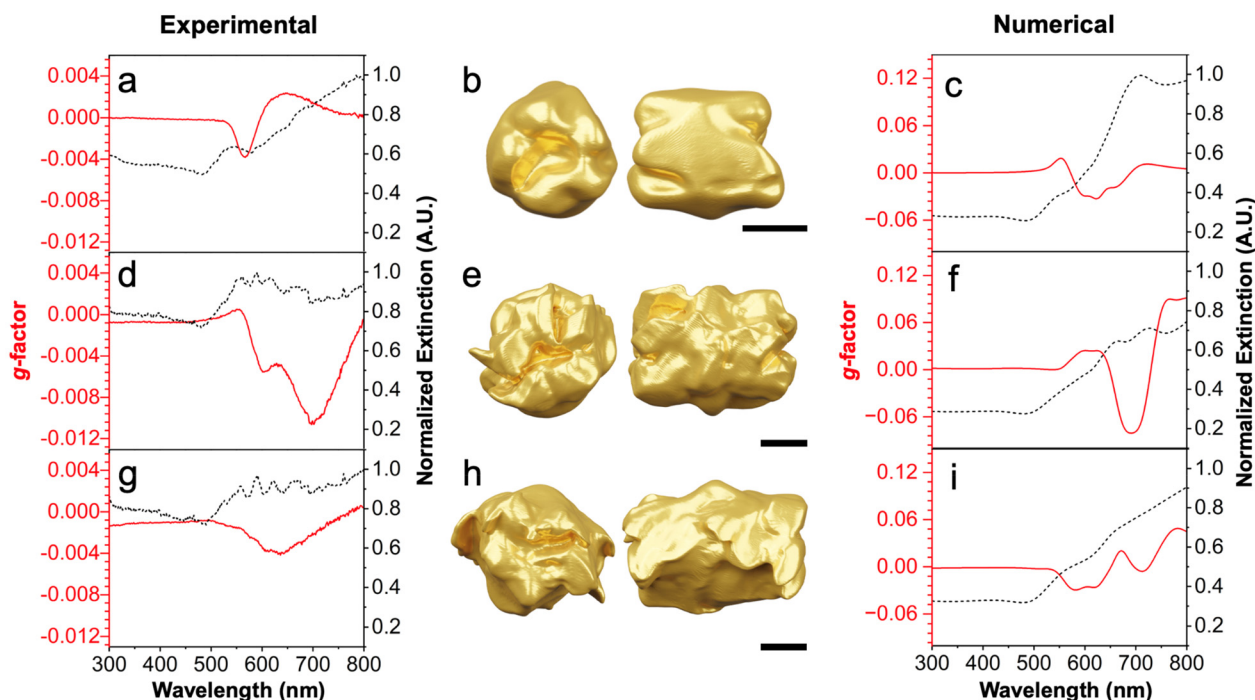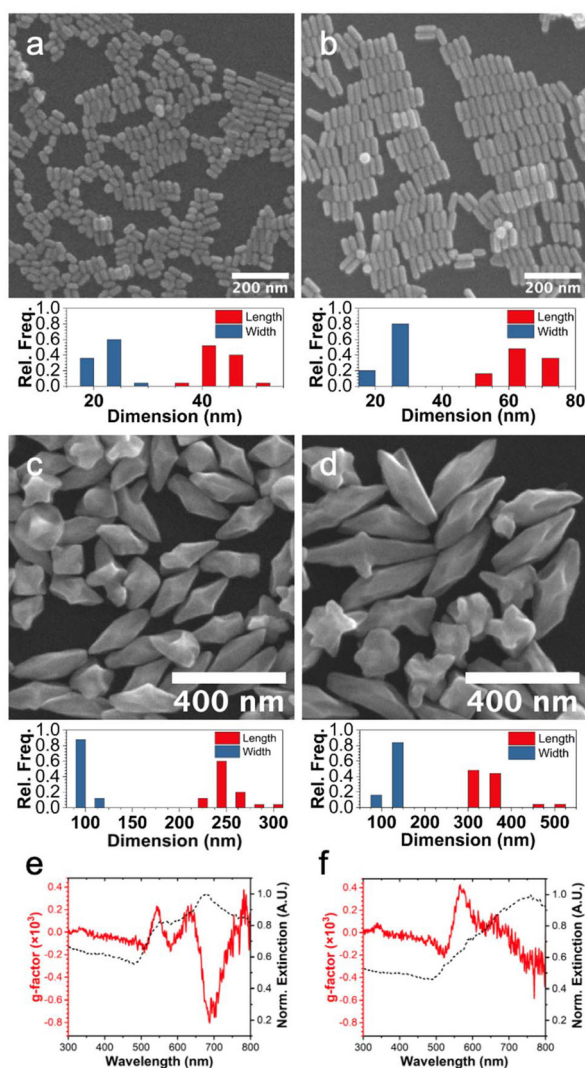

Fig. 4 (a, d and g) Experimental and (c, f and i) numerically calculated optical spectra for the 52-symmetric Au helicoids seeded from large pentatwinned rods of AR = ~1, 1.5, and 2.2 respectively. Tomographic reconstructions of individual 52-symmetric helicoids shown in (b, e and h) for the samples in Fig. 3d–f, respectively. Scale bars: 100 nm.

Fig. 5 (a and b) SEM images of small pentatwinned rods (width = ~20 nm) and AR of 2.2 and 3.2, respectively. (c and d) SEM images of the bipyramid products after overgrowth. Size distributions shown below the SEM image for each sample. (e and f) Experimental CD spectra for the bipyramid products.

synthesized from large pentatwinned rods which produce rods with 5-fold counterclockwise pinwheel ends. The formation of bipyramids from the small pentatwinned Au rods has been accounted for previously to the lower thermodynamic cost of propagating twin boundaries close to the C_5 axis.[31] The concavities emanating from the dihedral planes result from the use of the L-GSH as a chiral additive; these seeds grow into larger nanorods in the absence of L-GSH (Fig. S4†).

The optical properties of these bipyramid-like particles were investigated by UV-visible and CD spectroscopy and are shown in Fig. 5e and f. The g-factors of these particles are low due to only small chiral gap indentations, but the responses are distinct from the nonexistent g-factor of the achiral seeds (Fig. S5†).

Conclusions

We have successfully demonstrated the synthesis of 532- and 52-symmetric Au helicoids through seed-mediated growth from icosahedral and pentatwinned rod seeds, where the twin defects direct the expression of chiral features. By using high-symmetry icosahedral seeds, we achieve chiral helicoids of the highest platonic symmetry. The AR and size of pentatwinned seeds were also tuned to elucidate their impact on chiral particle growth, where smaller seed sizes led to smaller chiral gap volumes and larger seed sizes led to greater optical extinction. These features have opposite effects on g-factor and outline that next-generation syntheses of chiral NCs should strive to achieve large chiral gaps in small particle volumes. This research expands the family of accessible helicoid structures and provides design parameters for chiral NCs.

Author contributions

J.S.G. designed the experimental research. J.S.G. and M.P.P. synthesized and characterized seed and product particles. J.C. and J.S.G acquired STEM tilt images of 532- and 52-symmetric particles, and J.C. generated 3D tomographic reconstructions from these data. J.S.G performed all FDTD simulations and interpreted all data with supervision by S.E.S.

Data availability

Data for this article, including all electron microscopy, optical spectra, and size histograms are available at the materials data facility[33,34] at **https://doi.org/10.18126/eyca-8r61**.[35]

Conflicts of interest

There are no conflicts to declare.

Acknowledgements

References

1 J. García-Guirado, M. Svedendahl, J. Puigdollers and R. Quidant, *Nano Lett.*, 2018, **18**, 6279–6285.

2 S. D. Golze, S. Porcu, C. Zhu, E. Sutter, P. C. Ricci, E. C. Kinzel, R. A. Hughes and S. Neretina, *Nano Lett.*, 2021, **21**, 2919–2925.

3 J. Chen, X. Gao, Q. Zheng, J. Liu, D. Meng, H. Li, R. Cai, H. Fan, Y. Ji and X. Wu, *ACS Nano*, 2021, **15**, 15114–15122.

4 Y. Xia, Y. Xiong, B. Lim and S. E. Skrabalak, *Angew. Chem., Int. Ed.*, 2009, **48**, 60–103.

5 R. G. Weiner, M. R. Kunz and S. E. Skrabalak, *Acc. Chem. Res.*, 2015, **48**, 2688–2695.

6 J. S. Googasian, G. R. Lewis, Z. J. Woessner, E. Ringe and S. E. Skrabalak, *Chem. Commun.*, 2022, **58**, 11575–11578.

7 S. W. Im, E. Jo, R. M. Kim, J. H. Han and K. T. Nam, *Adv. Opt. Mater.*, 2023, **11**, 2300037.

8 C. J. DeSantis, A. C. Sue, M. M. Bower and S. E. Skrabalak, *ACS Nano*, 2012, **6**, 2617–2628.

9 N. H. Cho, H.-E. Lee, H.-Y. Ahn, Y. Y. Lee, S. W. Im, H. Kim and K. T. Nam, *Part. Part. Syst. Charact.*, 2019, **36**, 1900062.

10 K. A. Willets and R. P. Van Duyne, *Annu. Rev. Phys. Chem.*, 2007, **58**, 267–297.

11 W. A. Paiva-Marques, F. Reyes Gómez, O. N. Oliveira and J. R. Mejía-Salazar, *Sensors*, 2020, **20**, 944.

12 Y.-J. Kang, J.-W. Oh, Y.-R. Kim, J. S. Kim and H. Kim, *Chem. Commun.*, 2010, **46**, 5665.

13 H.-E. Lee, H.-Y. Ahn, J. Mun, Y. Y. Lee, M. Kim, N. H. Cho, K. Chang, W. S. Kim, J. Rho and K. T. Nam, *Nature*, 2018, **556**, 360–365.

14 P. R. Stevenson, M. Du, C. Cherqui, M. R. Bourgeois, K. Rodriguez, J. R. Neff, E. Abreu, I. M. Meiler, V. A. Tamma, V. A. Apkarian, G. C. Schatz, J. Yuen-Zhou and J. S. Shumaker-Parry, *ACS Nano*, 2020, **14**, 11518–11532.

15 S. Liu, X. Ma, M. Song, C.-Y. Ji, J. Song, Y. Ji, S. Ma, J. Jiang, X. Wu, J. Li, M. Liu and R.-Y. Wang, *ACS Nano*, 2021, **15**, 19535–19545.

16 B. Ni, M. Mychinko, S. Gómez-Graña, J. Morales-Vidal, M. Obelleiro-Liz, W. Heyvaert, D. Vila-Liarte, X. Zhuo, W. Albrecht, G. Zheng, G. González-Rubio, J. M. Taboada, F. Obelleiro, N. López, J. Pérez-Juste, I. Pastoriza-Santos, H. Cölfen, S. Bals and L. M. Liz-Marzán, *Adv. Mater.*, 2023, **35**, 2208299.

17 Y. Zheng, X. Li, L. Huang, X. Li, S. Yang, Q. Wang, J. Du, Y. Wang, W. Ding, B. Gao and H. Chen, *J. Am. Chem. Soc.*, 2023, **146**, 410–418.

18 K. Van Gordon, B. Ni, R. Girod, M. Mychinko, F. Bevilacqua, S. Bals and L. M. Liz-Marzán, *Angew. Chem., Int. Ed.*, 2024, **63**, e202403116.

19 L. D. Marks and L. Peng, *J. Phys.: Condens. Matter*, 2016, **28**, 053001.

20 Y. Xia, X. Xia and H.-C. Peng, *J. Am. Chem. Soc.*, 2015, **137**, 7947–7966.

21 Y. Tao, L. Sun, C. Liu, G. Yang, X. Sun and Q. Zhang, *Small*, 2023, **19**, 2301218.

22 L. Zhang, Y. Chen, J. Zheng, G. R. Lewis, X. Xia, E. Ringe, W. Zhang and J. Wang, *Angew. Chem., Int. Ed.*, 2023, **135**, e202312615.

23 X. Sun, L. Sun, L. Lin, S. Guo, Y. Yang, B. Zhang, C. Liu, Y. Tao and Q. Zhang, *ACS Nano*, 2024, **18**, 9543–9556.

24 X. Tian, Y. Lin, J. Dong, Y. Zhang, S. Wu, S. Liu, Y. Zhang, J. Li and Z. Tian, *Adv. Opt. Mater.*, 2017, **5**, 1700581.

25 A. Sánchez-Iglesias, N. Winckelmans, T. Altantzis, S. Bals, M. Grzelczak and L. M. Liz-Marzán, *J. Am. Chem. Soc.*, 2017, **139**, 107–110.

26 A. Sánchez-Iglesias, K. Jenkinson, S. Bals and L. M. Liz-Marzán, *J. Phys. Chem. C*, 2021, **125**, 23937–23944.

27 J. Schwartz, C. Harris, J. Pietryga, H. Zheng, P. Kumar, A. Visheratina, N. A. Kotov, B. Major, P. Avery, P. Ercius, U. Ayachit, B. Geveci, D. A. Muller, A. Genova, Y. Jiang, M. Hanwell and R. Hovden, *Nat. Commun.*, 2022, **13**, 4458.

28 P. B. Johnson and R. W. Christy, *Phys. Rev. B: Solid state*, 1972, **6**, 4370–4379.

29 Y. Xiong and Y. Xia, *Adv. Mater.*, 2007, **19**, 3385–3391.

30 B. Jin, M. L. Sushko, Z. Liu, X. Cao, C. Jin and R. Tang, *J. Phys. Chem. Lett.*, 2019, **10**, 1443–1449.

31 J. D. Smith, E. Bladt, J. A. C. Burkhart, N. Winckelmans, K. M. Koczkur, H. M. Ashberry, S. Bals and S. E. Skrabalak, *Angew. Chem., Int. Ed.*, 2020, **59**, 943–950.

32 Y. Sonnefraud, A. Leen Koh, D. W. McComb and S. A. Maier, *Laser Photonics Rev.*, 2012, **6**, 277–295.

33 B. Blaiszik, K. Chard, J. Pruyne, R. Ananthakrishnan, S. Tuecke and I. Foster, *JOM*, 2016, **68**, 2045–2052.

34 B. Blaiszik, L. Ward, M. Schwarting, J. Gaff, R. Chard, D. Pike, K. Chard and I. Foster, *MRS Commun.*, 2019, **9**, 1125–1133.

35 J. S. Googasian, M. P. Perkins, J. Chen and S. E. Skrabalak, *The Materials Data Facility*, 2024, DOI: **10.18126/eyca-8r61**.